Nano Research

Open Access

Research Article

Mn-doping-engineered $CsBi_3I_{10}$ lead-free perovskite photodetectors for high-performance blood oxygen monitoring

Jihui Wang, Guozhen Bai, Yufeng Hu, Zhe Yin ✉, and Aiwei Tang ✉

School of Physical Science and Engineering, Beijing Jiaotong University, Beijing 100044, China

Cite this article: *Nano Research*, **2026**, *19*, 94908478. https://doi.org/10.26599/NR.2026.94908478

ABSTRACT: Lead-free perovskites are promising for photodetector applications due to their excellent optoelectronic properties and low toxicity. However, the performance of perovskite-based photodetectors is often limited by defects in the films, leading to non-radiative recombination and reducing carrier mobility. In this work, we report the significant performance enhancement of $CsBi_3I_{10}$ perovskite photodetectors through Mn doping. Mn-doped $CsBi_3I_{10}$ films were prepared in an air environment, which still shows good stability. Structural and photoelectronic characterizations confirm that Mn doping effectively passivates defects, suppresses non-radiative recombination, and reduces the dark current. Furthermore, this doping strategy leads to a remarkably weak light detection feature and high reproducibility of the photodetectors. The optimized device achieves a responsivity of 1.11 A/W, a specific detectivity of 1.62×10^{12} Jones, a fast response time of 4.53 (rise) and 1.47 μs (decay) under 650 nm illumination. Considering its special response spectrum and fast response under low-light conditions, a blood oxygen saturation monitoring system was successfully built on the Mn-doped $CsBi_3I_{10}$ perovskite, achieving high sensitivity. This work not only demonstrates an effective doping strategy for improving the performance of lead-free perovskite photodetectors but also highlights their potential as low-toxicity candidates for wearable health monitoring.

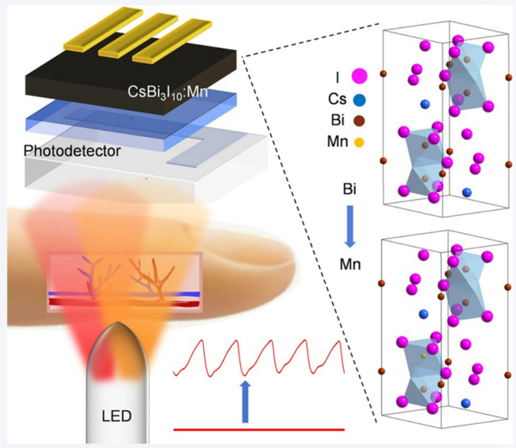

KEYWORDS: Pb-free perovskite, Mn doping, stability, photodetectors, blood oxygen monitoring

1 Introduction

High-performance photodetectors play an indispensable role in numerous optoelectronic applications in both civilian and military fields, such as biomedical imaging and optical communication [1–3]. Commercial semiconductors have achieved good detection performance. At present, demands have been put forward for the performance of high-performance detectors. A new generation of high-performance photodetectors needs to be developed. In recent years, lead halide perovskites have stood out due to their excellent semiconductor properties, including high light absorption coefficient, long carrier diffusion length, and easily adjustable bandgap. Lead halide perovskites have made significant progress in the field of optoelectronics [4, 5]. However, the toxicity and instability of Pb remain the main obstacle to the commercialization of perovskites. Therefore, finding alternatives to Pb is indispensable. Although Sn-based perovskite has a small bandgap and can achieve a rapid response up to 373 ns [6], Sn^{2+} is easily oxidized to Sn^{4+} in air [7]. Bi and Pb are in the same period, have similar radii, and Bi-based perovskites have excellent environmental stability, making them an excellent substitute. Liu et al. used $Cs_2AgBiBr_6$ single crystal doped with Fe^{2+} for near-infrared response (1350 nm) [8]. Hao et al. proposed a self-powered photodetector based on $CsBi_3I_{10}/SnO_2$ heterojunction, achieving a switching ratio of up to 2.33×10^5 [9]. Wei et al. successfully prepared a flexible $CsBi_3I_{10}$ photodetector by doping conductive polymer polyvinylcarbazole. After 1000 cycles of bending tests, the photocurrent still remained at 80% [10].

Compared with conventional Pb-based perovskites, $CsBi_3I_{10}$ perovskite exhibits moderate photoelectric performance due to its low defect tolerance and severe non-radiative recombination, resulting in lower photoelectric conversion efficiency than Pb-based perovskites. The doping of transition metal ion Mn is a known and effective method that can improve the photophysical properties and

Received: December 5, 2025; **Revised:** January 18, 2026
Accepted: January 21, 2026

✉Address correspondence to Aiwei Tang, awtang@bjtu.edu.cn; Zhe Yin, zheyin@bjtu.edu.cn

stability of perovskite [11–13]. The Mn doping has been widely used in conventional semiconductors. Recently, significant progress has been made in doping Mn into Pb-based, In-based, and Cu-based perovskite materials [14–17]. The experimental results show that Mn doping also has significant beneficial effects in Bi-based perovskite systems.

In this study, we improved the quality of $CsBi_3I_{10}$ perovskite and enhanced carrier mobility through Mn doping. Under the illumination of a 650-nm light source, the Mn-doped device exhibits a responsivity of 1.11 A/W, a specific detection rate of 1.62×10^{12} Jones, and a response time of 4.53/1.47 μs. The low-toxicity, fast response time, and unique sensitivity to low light of Mn-doped $CsBi_3I_{10}$ perovskites are desirable for detecting weak signals such as blood oxygen monitoring. A blood oxygen detection system we built for accurately measuring heart rate and blood oxygen saturation of the human body. The Pb-free $CsBi_3I_{10}$ photodetectors with suppressed defects show great potential in blood oxygen detection.

2 Experimental

2.1 Materials

The materials used in the experiments included cesium iodide (CsI, aladdin, 99.9%), bismuth iodide (BiI_3, aladdin, 99.9%), manganese chloride ($MnCl_2$, aladdin, 99%), N,N-dimethylformamide (DMF, aladdin, 99.5%), dimethyl sulfoxide (DMSO, aladdin, 99.5%), trichloromethane ($CHCl_3$, Beijing Tong Guang Fine Chemicals Company, > 99%), and poly(9-vinylcarbazole) (PVK, aladdin, average M_n 40,0000–50,0000).

2.2 Preparation of $CsBi_3I_{10}$ perovskite precursor

0.8 mmol CsI and 2.4 mmol BiI_3 were dissolved in 1 mL of a mixed solution (DMF:DMSO = 9:1, V/V). The mixture was stirred at 70 °C for 1 h and filtered using a 0.22 μm polytetrafluoroethylene filter. $MnCl_2$ (0.01, 0.03, and 0.05 mmol) was added during the above process.

2.3 Device fabrication

The glass substrate with indium tin oxide (ITO) was rinsed sequentially with deionised water, isopropanol and ethanol in turn for 15 min. The residual liquid on the substrate was flushed out with N_2, and the glass substrate was treated with ultraviolet (UV) ozone for 15 min. Firstly, 60 μL of poly(3,4-ethylenedioxythiophene): poly(styrenesulfonate) (PEDOT:PSS) was spin-coated at 5000 rpm for 30 s, and then annealed under vacuum at 120 °C for 30 min. Then, 60 μL of $CsBi_3I_{10}$ perovskite precursor solution was spin-coated at 4000 rpm for 60 s. 100 μL of anti-solvent chloroform was added at the 10th second. The solution was then annealed under vacuum at 100 °C for 30 min. Finally, a layer of Au electrode was thermally evaporated on the perovskite film. The active layer area is 4.5 mm^2.

2.4 Characterization

The morphology was characterized by scanning electron microscopy (SEM) using field emission SEM (FE-SEM, FEI Quanta 650, 3 kV). The X-ray diffraction (XRD) patterns were obtained by a Bruker D8 advance diffractometer using a Cu Kα radiation source (λ = 1.54056 Å). The absorption spectra were recorded using a HR2000CG-UVNIR spectrometer from Ocean Optics. The light source is a 650 nm laser (Cnilaser, MRL-III-650 nm). The external quantum efficiency (EQE) was measured by Zurich's Solar Cell QE/IPCE Measurement System. The response time of the device was measured by a lock-in amplifier (Zurich Instruments, MFLI).

3 Results and discussion

Figure 1(a) shows the fabrication process of a Mn^{2+} doped $CsBi_3I_{10}$ ($CsBi_3I_{10}$:Mn) based photodetector by sequentially spin-coating a hole transport layer PEDOT:PSS, active layer $CsBi_3I_{10}$ perovskite film, and finally thermally evaporating a layer of Au electrodes. The obtained device structure is glass/ITO/PEDOT:PSS/$CsBi_3I_{10}$:Mn/Au. The ITO electrode is transparent. The absorption of visible infrared light is very low, and the work function is 4.7 eV, which is desirable for $CsBi_3I_{10}$:Mn. The valence band energy level of

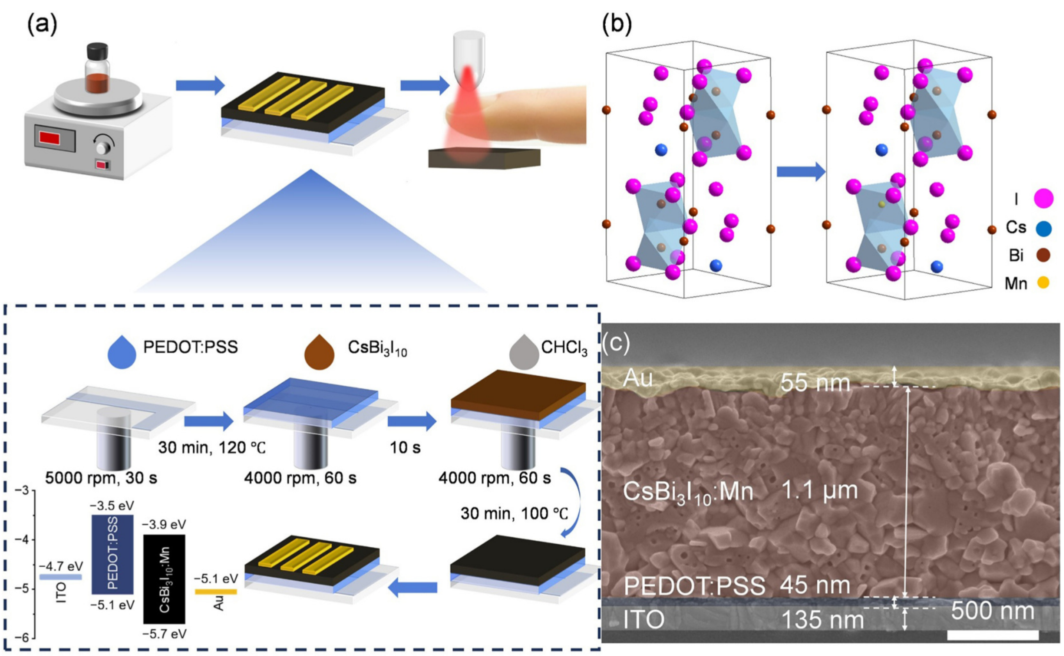

Figure 1 (a) Photodetector preparation flow. (b) Mn doping structure. (c) SEM image of cross section of the photodetector.

PEDOT:PSS is between ITO and $CsBi_3I_{10}$, which can promote hole migration, and fill uneven areas to improve the smoothness of $CsBi_3I_{10}$:Mn perovskite thin films. In this paper, Mn^{2+} is successfully doped in $CsBi_3I_{10}$ perovskite (Fig. 1(b)) to reduce the surface defects of perovskite and improve carrier mobility. Figure 1(c) shows a cross-sectional SEM of a $CsBi_3I_{10}$:Mn perovskite photodetector with thicknesses of ITO, PEDOT:PSS, $CsBi_3I_{10}$:Mn, and Au are 135, 45, 1.1, and 55 nm, respectively.

The addition of Mn^{2+} can significantly regulate the surface flatness of $CsBi_3I_{10}$ thin films, which is important for the following device fabrication. Figures 2(a)–2(c) show that as the Mn doping content increases, the morphology changes. The morphology of the film with a doping concentration of 0.01 mol/L ($CsBi_3I_{10}$:0.01Mn) is similar to that without doping, while the film with a doping concentration of 0.05 mol/L ($CsBi_3I_{10}$:0.05Mn) shows obvious irregularity. Figure S1 in the Electronic Supplementary Material (ESM) shows the energy dispersive X-ray spectroscopy (EDS) of the surface of $CsBi_3I_{10}$:0.05Mn thin film, indicating a relatively uniform distribution of Mn element. Table S1 in the ESM records that the principle of Mn accounts for 1%. X-ray photoelectron spectroscopy (XPS) characterization was performed on perovskite films with different Mn doping concentrations. Figures 2(d) and 2(e) show that with the increasing Mn doping, the binding energy of Bi 4f and Mn 2p orbitals shift to lower values, indicating an enhanced electron cloud density. This is attributed to the replacement of Bi^{3+} by Mn^{2+}, which creates localized negative charge centers that can be compensated by the formation of positively charged iodine vacancies to preserve overall charge neutrality. Figure 2(e) shows that the binding energy of the Mn 2p orbital is significantly lower compared to the literature. It can be ascribed to the difference in the anion. The electronegativity of Cl^- and O^{2-} is higher than that of I^-, and they have a stronger ability to adsorb electrons. In $CsBi_3I_{10}$, the anion is I^- has a high electron-donating capacity [11, 13, 18]. Mn^{2+} is affected, showing a decrease in the binding energy of Mn 2p orbitals. Figure 2(f) shows the absorption spectra of Mn-doped $CsBi_3I_{10}$ with different concentrations of Mn. With the increasing Mn, the absorption edge of $CsBi_3I_{10}$ is blueshifted, with the maximum blueshift of 10 nm in $CsBi_3I_{10}$:0.05Mn samples. Furthermore, to compare the energy band of the samples, the ultraviolet photoelectron spectroscopy (UPS) characterization of $CsBi_3I_{10}$ doped with different concentrations of Mn was performed (Fig. S2 in the ESM). It was found that the valence band energy levels of the

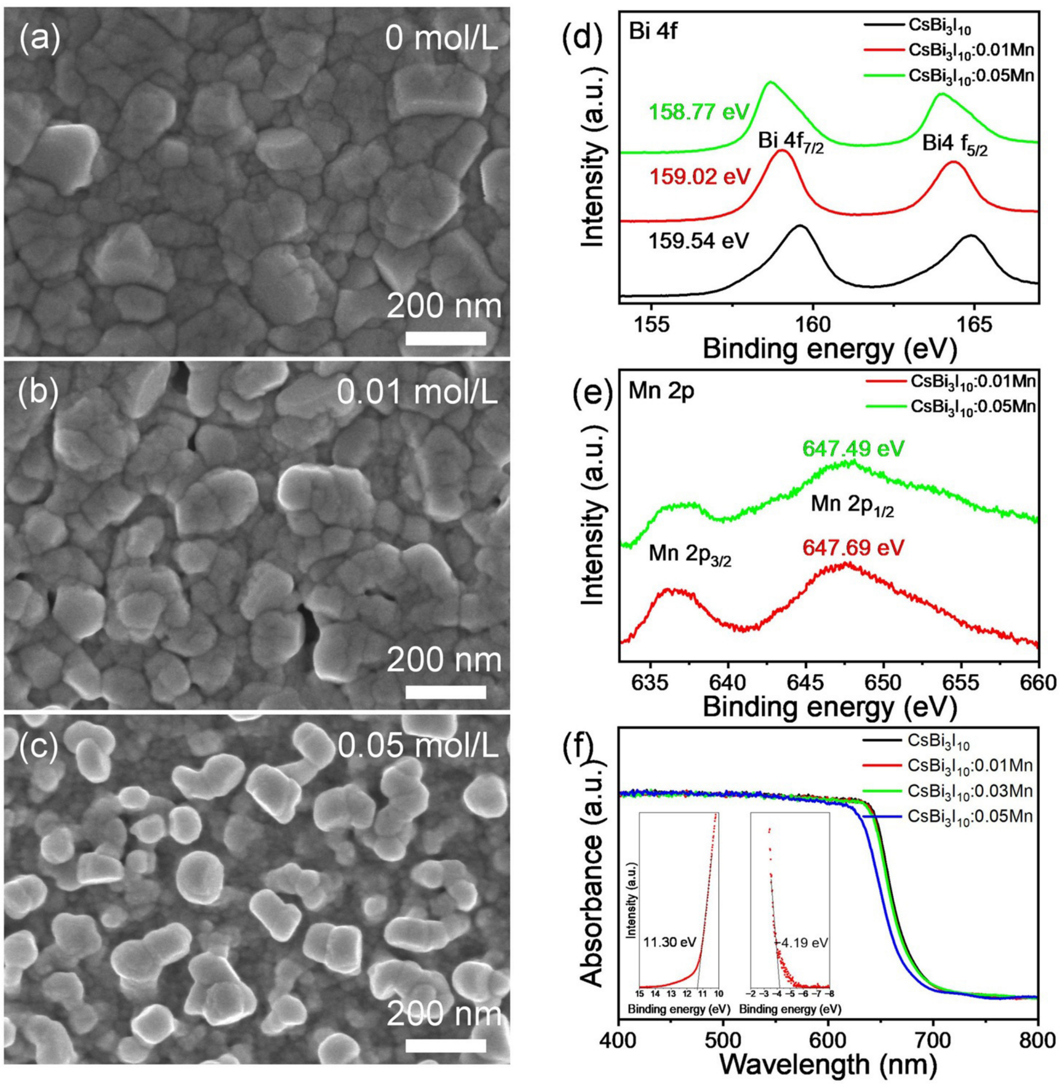

Figure 2 SEM of $CsBi_3I_{10}$ perovskite films with different Mn concentrations: (a) $CsBi_3I_{10}$, (b) $CsBi_3I_{10}$:0.01Mn, and (c) $CsBi_3I_{10}$:0.05Mn. XPS of different concentrations of Mn-doped $CsBi_3I_{10}$ perovskite films: (d) Bi 4f and (e) Mn 2p. (f) Absorption spectra.

perovskites decreased slightly with increasing Mn content.

Mn^{2+} doping was found to significantly enhance the performance of the $CsBi_3I_{10}$ photodetector. In a low-light condition, the photocurrent of the Mn-doped $CsBi_3I_{10}$ photodetector significantly increases. Figure 3(a) shows that the device is responsive in the spectra of 400–700 nm (28 μW/cm²). It is worth noting that in the spectra of 550–650 nm, the external quantum efficiency (EQE) of the $CsBi_3I_{10}$:0.01Mn device is approximately 10% higher than that of the undoped device.

For the device performance tests, the light source was a 650 nm laser at 5 mW/cm², and the operating voltage was 1 V reverse biased. Unless mentioned in this paper, these are the test conditions. The switching ratio (I_{on}/I_{off}) is defined as the ratio of the photocurrent (I_{photo}) to the dark current (I_{dark}). $I_{on}/I_{off} = I_{photo}/I_{dark}$, where $I_{photo} = I_{light} - I_{dark}$. The Mn doping can reduce the defects of perovskite, thus reducing the I_{dark} of the device and increasing the I_{on}/I_{off}. Space charge limited current (SCLC) experiment was carried out to measure the trap state density of charge carriers in perovskite thin films (Fig. S3 in the ESM). The experimental results have proven the surface defects are reduced by Mn doping. To show the average parameters of the photodetectors, we tested 10 devices. The standard deviation of I_{on}/I_{off} values for Mn-doped devices is shown to be significantly smaller than that of the undoped devices in Fig. 3(b), indicating Mn doping leads to more stable device performance with high reproducibility. The $CsBi_3I_{10}$:0.01Mn device has the highest I_{on}/I_{off}. The results of the repeated experiments were consistent with them (Fig. S4 in the ESM). The I_{on}/I_{off} of the photodetector decreases with increasing Mn doping concentration. This observation is consistent with the previous SEM image results, which indicate that excessive Mn content leads to a rough morphology of $CsBi_3I_{10}$, while insufficient Mn content has a minimal impact on the device. Figure S5 in the ESM shows the switching ratio of Mn-doped devices with different concentrations after 13 months. It can be proven that the $CsBi_3I_{10}$:0.01Mn device has the best stability.

Figure 3(c) shows the typical I–V curves of different Mn-doped devices, revealing a slight increase in I_{photo} and a decrease in I_{dark} for the $CsBi_3I_{10}$:0.01Mn device. The I_{dark} of $CsBi_3I_{10}$ and $CsBi_3I_{10}$:0.01Mn were 23 and 18 nA, respectively, and the I_{on}/I_{off} were 1270 and 1370, respectively. In addition, the I_{photo} zero shift phenomenon diminishes as the Mn doping concentration increases. It is because the carrier concentration in $CsBi_3I_{10}$ is significantly lower than that in PEDOT:PSS, leading to the formation of a built-in electric field due to the free diffusion of hole carriers [19, 20]. The carrier concentration of $CsBi_3I_{10}$ increases with increasing Mn-doped concentration [21, 22]. The concentration difference between $CsBi_3I_{10}$ and PEDOT:PSS is reduced, leading to a decreased built-in electric field. In this paper, the current I–V curves of $CsBi_3I_{10}$ and $CsBi_3I_{10}$:0.01Mn devices were also tested at different optical power densities (Figs. S6(a) and S6(b) in the ESM).

Linear dynamic range (LDR) is the range over which the

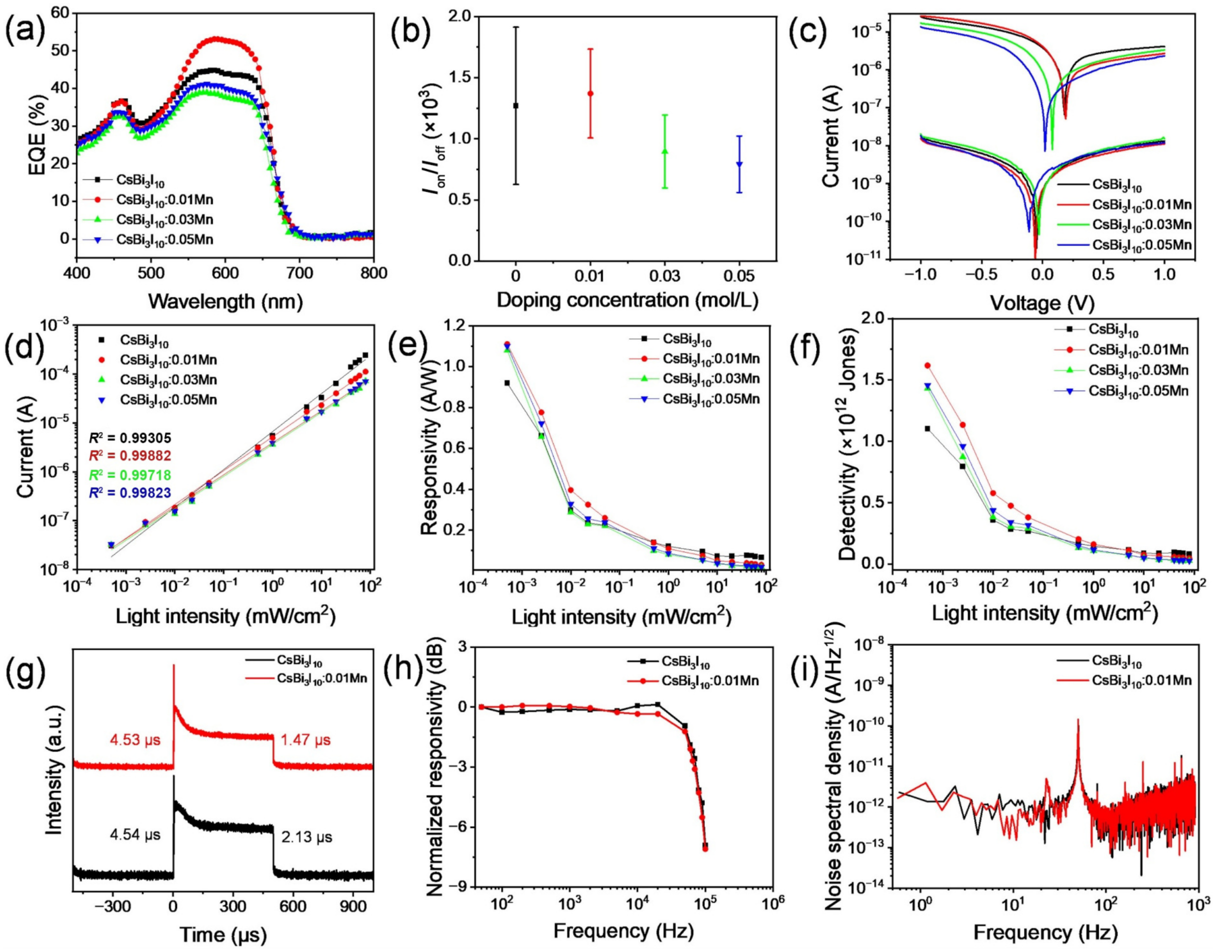

Figure 3 Characterization of the performance of $CsBi_3I_{10}$ photodetectors with different Mn concentrations: (a) EQE, (b) I_{on}/I_{off}, (c) I–V curves, (d) LDR, (e) R, (f) D^*, (g) response time, (h) −3 dB, and (i) NSD.

photoelectric conversion of a photodetector remains linear. LDR = $20\lg(P_{max}/P_{min})$, where P_{max} is the maximum incident optical power in the linear range, and P_{min} is the minimum incident optical power in the linear range. P_{max} is 80 mW/cm^2, and P_{min} is 0.5 μW/cm^2 in Fig. 3(d). The value of LDR is 104 dB. The data were fitted, and the $CsBi_3I_{10}$:0.01Mn device exhibited the best fit with a fitting coefficient R^2 value of 0.99882. Figures S6(c) and S6 (d) in the ESM show the I_{light} at different optical powers and their compliance with the LDR results.

Responsivity (R) is also often referred to as sensitivity, $R = I_{photo}/PS$, where P is the incident light intensity, S is the effective illumination area. Figure 3(e) shows that the Mn-doped device exhibits higher response with R up to 1.11 A/W. As the optical power increases, the responsivity of Mn-doped devices is lower than that of undoped devices. Overdose Mn introduces doping level in the band gap. The doping of Mn promotes carrier separation and transport in low light, reduces non-radiative complexation, enhances the effective carrier concentration under low-light condition, and improves the responsivity of Mn-doped devices at low optical power density. At high optical power density, the concentration of photogenerated carriers far exceeds the accommodating capacity of Mn trap states. Mn changes into the recombination center, accelerating the annihilation of electron–hole pairs. This leads to a decrease in the responsivity of Mn-doped devices under intense light.

The specific detection rate D^* describes the sensitivity of the photodetector to weak irradiance (Eq. (1))

$$D^* = RS^{1/2}/2eI_{dark}^{1/2} \tag{1}$$

Mn doping suppresses the I_{dark} of the photodetector and improves the detecting performance of the device, especially under illumination with low optical power density. Figure 3(f) shows that the D^* of $CsBi_3I_{10}$:0.01Mn device is up to 1.62×10^{12} Jones (1 Jones = 1 cm·Hz$^{1/2}$/W).

Figures 3(g)–3(i) show the time-dependent optical properties. Figure 3(g) shows the response times of the $CsBi_3I_{10}$ and $CsBi_3I_{10}$:0.01Mn devices, of which the response and recovery time are 4.54/2.13 μs and 4.53/1.47 μs. Figure 3(h) shows that the cut-off frequency (−3 dB) of both the $CsBi_3I_{10}$ and $CsBi_3I_{10}$:0.01Mn devices is 70 kHz. Figure 3(i) shows the noise spectral density (NSD), which is the noise power density per unit bandwidth [23, 24] (the unit is A/Hz$^{1/2}$) (Eq. (2))

$$\mathrm{NSD} = (A^2/Fn)^{1/2} \tag{2}$$

Performing a fast Fourier transform on a set of I_{dark} data can obtain a new set of data. Where A is the amplitude, F is the I_{dark} sampling frequency, and n is the number of data for the amplitude. The graph shows a distinct peak at 50 Hz, which is the ambient alternating current signal interference. Figure S7 in the ESM shows the I_{dark} and its noise spectral density for different sampling frequencies. In comparison with other perovskite photodetectors, our research results are at an upstream level in the reported work (Table S2 in the ESM).

The stability of $CsBi_3I_{10}$ perovskite is tested by its crystal structure and photodetector performances. Figures 4(a) and 4(b) show the X-ray diffraction (XRD) patterns of $CsBi_3I_{10}$ thin films doped with Mn, measured on the 1st day and 22nd day. Figure 4(a) shows that Mn doping changed the relative intensity of the two strongest peaks (003) and (005). Specifically, as the Mn content increases, the intensity ratio of (003) to (005) gradually increases, indicating that Mn doping changes the growth orientation of $CsBi_3I_{10}$ perovskite. Comparing Figs. 4(a) and 4(b), no significant changes in XRD patterns are observed over time, confirming the excellent stability of $CsBi_3I_{10}$ perovskite films. Figures 4(c) and 4(d) show the long-term stability tests of I_{photo} and I_{on}/I_{off}. At a power density of 5 mW/cm^2, the I_{photo} decreases with increasing Mn doping concentration. However, in terms of standard deviation, the quality of $CsBi_3I_{10}$:Mn devices exhibits excellent stable performance. Figure S8 in the ESM shows a detailed comparison of the I_{dark}, I_{photo}, I_{on}/I_{off}, and their normalized values for photodetectors with different Mn concentrations. Figure 4(e) shows the cyclic I_{photo} response of the $CsBi_3I_{10}$:0.01Mn device for 1 h continuous operation, retaining 87% of its initial I_{photo}. Figure 4(f) shows a magnified view of a segment from Fig. 4(e), highlighting the details.

The Mn-doped $CsBi_3I_{10}$ photodetector shows great advantages in detecting weak signals, making it suitable for applications such as blood oxygen detection. Photoplethysmography (PPG) is a non-invasive optical sensing method based on Lambert-Beer's law, used to monitor blood volume changes in subcutaneous tissue [25–28]. The basic principles are discussed in the Supporting Information. This study shows the application of $CsBi_3I_{10}$ photodetectors in measuring human heart rate (HR) and blood oxygen saturation (SpO_2). Figure 5(a) shows that light of fixed intensity becomes pulsed light after passing through the fingertip. The photodetector converts the pulsed optical signal into an electrical signal. An integrated circuit AFE4490EVM and its graphical user interface (GUI) software were used to capture and process the electrical signals while controlling the alternating illumination of the LEDs (620/660 nm) [29]. Figures 5(b) and 5(c) show the PPG signals, HR, absorbed light ratio (R_{os}) and SpO_2 values based on $CsBi_3I_{10}$ and $CsBi_3I_{10}$:0.01Mn photodetectors. Comparing the PPG signals of the two photodetectors, it was found that the converted electrical signals of the $CsBi_3I_{10}$:0.01Mn device (11.3 mV) were significantly higher than those of the $CsBi_3I_{10}$ device (6.2 mV). Specifically, at 660 nm light, both the direct current (DC) and alternating current (AC) signals of the $CsBi_3I_{10}$:0.01Mn device are approximately twice those of the $CsBi_3I_{10}$ device. This is attributed to the enhanced sensitivity of Mn-doped devices to weak light. The calculated HR and SpO_2 from the five PPG signals from the $CsBi_3I_{10}$ photodetector are 77–79 beats per minute and 96%–99%, and the average values are 78.29 beats per minute and 98.34%, respectively. In contrast, for the $CsBi_3I_{10}$:0.01Mn photodetector, the calculated HR and SpO_2 from the five PPG signals are 78–85 beats per minute and 93%–98%, the average values are 80.42 beats per minute and 96.47%, respectively. Despite slight variations, the results from both detectors are comparable, showing the potential of $CsBi_3I_{10}$:Mn photodetectors for healthcare monitoring.

4 Conclusion

In conclusion, we successfully fabricated Mn-doped $CsBi_3I_{10}$ photodetectors and took the advantage of their weak light detection and high reproducibility for application in percutaneous oxygen monitoring. For materials design, Mn doping was found to effectively smooth the surface of the $CsBi_3I_{10}$ film. Furthermore, to enhance interfacial charge transfer, charge transport layers were added into the device with the structure of ITO/PEDOT:PSS/$CsBi_3I_{10}$/Au. It can be concluded that the optimized $CsBi_3I_{10}$:0.01Mn device exhibits the best performance,

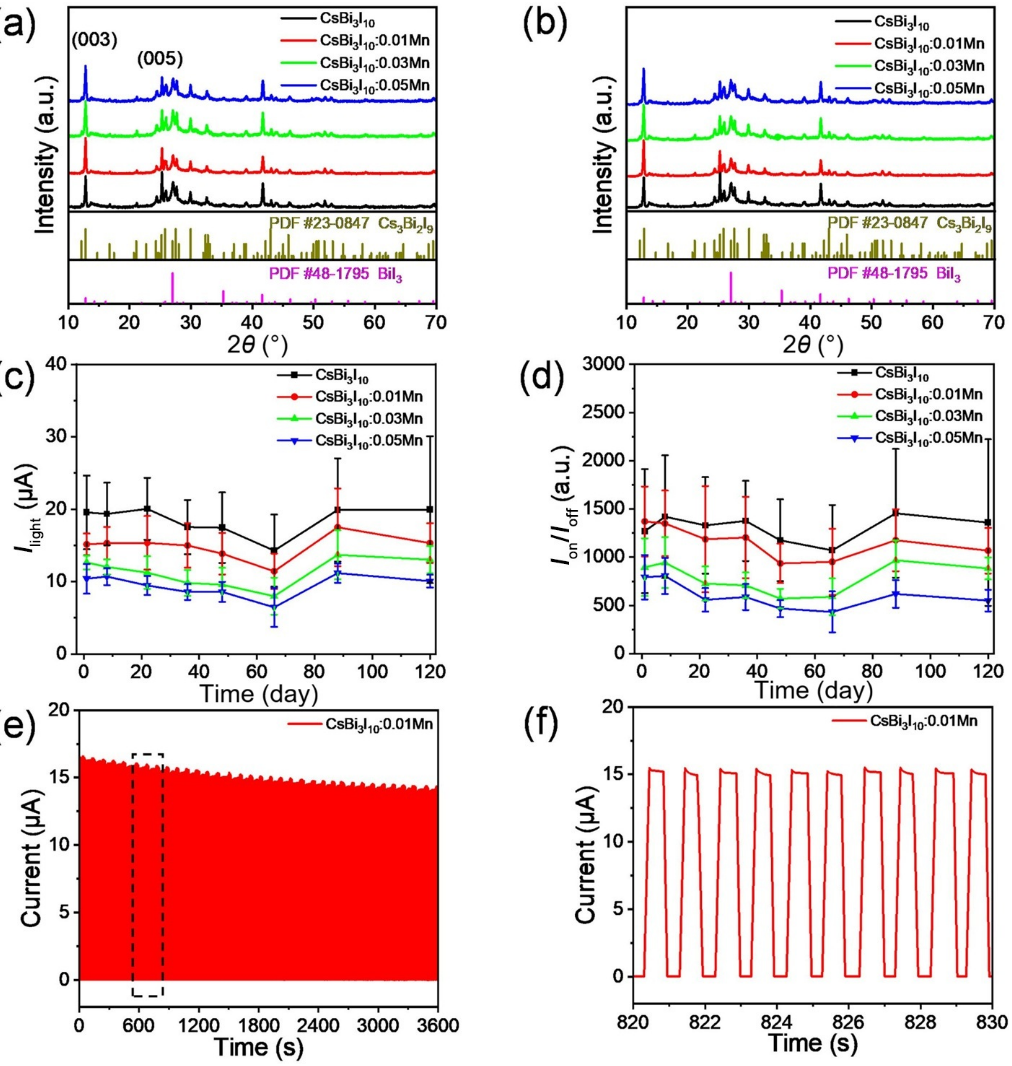

Figure 4 XRD of Mn-doped $CsBi_3I_{10}$ films at the: (a) 1st day and (b) 22nd day. Long-term performances: (c) I_{photo} and (d) I_{on}/I_{off}. (e) Cyclic curve of I_{on} and I_{off} in $CsBi_3I_{10}$:0.01Mn devices, (f) I_{photo} curves taken from part (e).

achieving a responsivity of 1.11 A/W and an impressively high specific detectivity of 1.62×10^{12} Jones, which outperforms those of the undoped device for weak light detection. The standard deviation of the optoelectronic performance of Mn-doped devices is significantly lower than that of undoped devices, indicating that the reproducibility of device is greatly improved. Moreover, Mn-doped devices maintain their performance levels in terms of response time, cut-off frequency, and noise spectral density without any degradation. Finally, a transmission mode pulse oximeter system based on the detection range of Mn-doped $CsBi_3I_{10}$ was developed, which can non-invasive monitor human heart rate and pulse oxygen saturation. This Mn-doped strategy can shed light on the practical application of Pb-free perovskites with high sensitivity and reproducibility.

Electronic Supplementary Material: Supplementary material (further details of mterials, characterization, analytical methods, and other experimental figures and tables (Figs. S1–S7, Tables S1 and S2)) is available in the online version of this article at https://doi.org/10.26599/NR.2026.94908478.

Data availability

All data needed to support the conclusions in the paper are presented in the manuscript and the Electronic Supplementary Material. Additional data related to this paper may be requested from the corresponding author upon request.

Acknowledgements

This work was supported by the National Natural Science Foundation of China (Nos. 12574429, 62105019, and 61974009).

Declaration of competing interest

All the contributing authors report no conflict of interests in this work.

Author contribution statement

J. H. W.: Validation, writing manuscript, experimental design. G. Z. B. and Y. F. H.: Methodology, resources. Z. Y.: Data curation, experimental design, writing manuscript, funding acquisition. A. W. T.: Project administration. All the authors have approved the

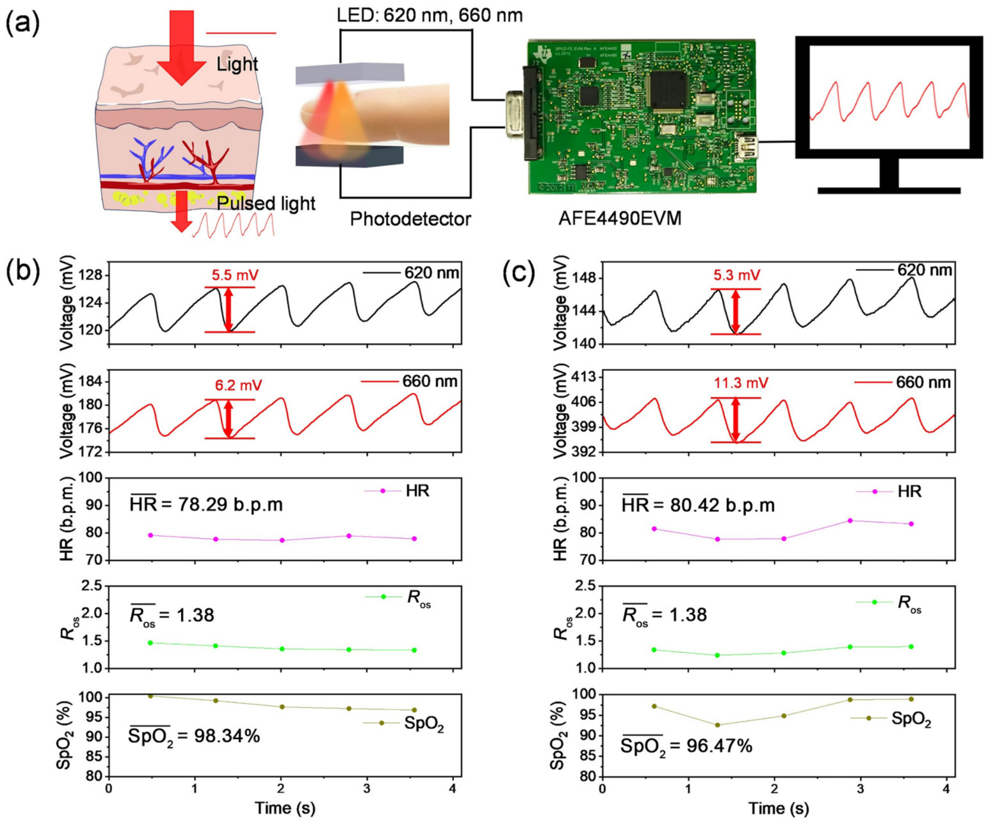

Figure 5 (a) Demonstration of blood oxygen detection. (b) Blood oxygen data of devices based on undoped $CsBi_3I_{10}$ photodetectors. (c) Blood oxygen data of devices based on $CsBi_3I_{10}$:0.01Mn photodetectors.

final manuscript.

Use of AI statement

During the preparation of this work, the authors used DeepSeek in order to check the grammar and spelling. After using this tool, the authors reviewed and edited the content as needed and take full responsibility for the content of the publication.

References

[1] Li, Y.; Shi, Z. F.; Liang, W. Q.; Ma, J. L.; Chen, X.; Wu, D.; Tian, Y. T.; Li, X. J.; Shan, C. X.; Fang, X. S. Recent advances toward environment-friendly photodetectors based on lead-free metal halide perovskites and perovskite derivatives. *Mater. Horiz.* **2021**, *8*, 1367–1389.

[2] Xiao, H. B.; Liu, T. H.; Wei, X. F.; Liu, S. C.; Meng, X. Y.; Zhao, Y. C. Pyrazole-engineered low-defect tin halide perovskites for ultraweak-light imaging and pixel-Level image fusion. *Adv. Funct. Mater.* **2026**, *36*, e09196.

[3] Yang, Z. C.; Liu, J. J.; Bao, H. T.; Liu, Z. H.; Wang, Z. W.; Li, X. D.; Chen, Z. H.; Zhang, G. F.; Chen, R. Y.; Hu, J. Y. et al. A monolithically integrated near-infrared imager with crystallization- and oxidation-modulated tin-lead perovskites. *Light: Sci. Appl.* **2025**, *14*, 304.

[4] Wang, Y.; Xu, B. T.; Song, Z. Y.; Liu, W. Z.; Shen, W. S.; Zhou, D. Y.; Wang, Y. K.; Liao, L. S. Dipole regulation enables efficient near-infrared perovskite quantum dots photodetector. *Adv. Funct. Mater.* **2026**, *36*, e14588.

[5] Cheng, L.; Wang, F.; Wang, D. S.; Liu, H. Q.; Meng, F. N.; Wang, G. Q. Additive engineering-assisted perovskite crystallization modulation and *in situ* buried interface healing for stable and efficient planar $CsPbI_3$ perovskite solar cells. *ACS Appl. Mater. Interfaces* **2025**, *17*, 47252–47259.

[6] Lv, Y. B.; Cen, G. B.; Li, W. J.; Zhao, C. X.; Mai, W. Highly sensitive fast-response near-infrared photodetectors based on triple cation Sn–Pb perovskite for pulse oximetry system. *Sci. China Mater.* **2023**, *66*, 4704–4710.

[7] Cao, F. R.; Tian, W.; Wang, M.; Wang, M.; Li, L. Stability enhancement of lead-free $CsSnI_3$ perovskite photodetector with reductive ascorbic acid additive. *InfoMat* **2020**, *2*, 577–584.

[8] Liu, G. H.; Zhang, Z. H.; Wu, C. C.; Zhang, Y. Q.; Li, X. D.; Yu, W. J.; Yao, G. J.; Liu, S. M.; Shi, J. J.; Liu, K. H. et al. Extending absorption of $Cs_2AgBiBr_6$ to near-infrared region (≈ 1350 nm) with intermediate band. *Adv. Funct. Mater.* **2022**, *32*, 2109891.

[9] Hao, D. D.; Liu, D. P.; Shen, Y. K.; Shi, Q. Q.; Huang, J. Air-stable self-powered photodetectors based on lead-free $CsBi_3I_{10}/SnO_2$ heterojunction for weak light detection. *Adv. Funct. Mater.* **2021**, *31*, 2100773.

[10] Wei, C. C.; Wang, J. H.; Wang, L. J.; Zhao, J. X.; Yin, Z.; Tang, A. W. Highly efficient flexible photodetectors based on Pb-free $CsBi_3I_{10}$ perovskites. *ACS Appl. Mater. Interfaces* **2024**, *16*, 28845–28852.

[11] Rafie, M. S. M.; Mahat, A. M.; Halizan, M. Z. M.; Musyarofah, M.; Mohamed, Z. Impact of Mn doping on structural, optical and dielectric properties of titanium-based double perovskite $La_2CuTi_{1-x}Mn_xO_6$. *Ceram. Int.* **2025**, *51*, 11437–11454.

[12] Guo, R. Q.; Meng, J.; Lin, W. H.; Liu, A. Q.; Pullerits, T.; Zheng, K. B.; Tian, J. J. Manganese doped eco-friendly $CuInSe_2$ colloidal quantum dots for boosting near-infrared photodetection performance. *Chem. Eng. J.* **2021**, *403*, 126452.

[13] Sheng, Y. Y.; Chen, P.; Gao, Y. P.; He, Y.; Li, J. C.; Muhammad; Xie, X.; Cheng, C.; Yang, J. T.; Chang, Y. J. et al. Tuneable efficient white emission of Sb^{3+}/Mn^{2+} Co-doped lead-free perovskites for single-component white light-emitting diodes. *ACS Appl. Mater. Interfaces*

2024, *16*, 19175–19183.
[14] A, M.; Suresh, S.; Subramaniam, M. R.; Batabyal, S. K. Synthesis of Mn^{2+}:CsPb $(Br_{1-x}Cl_x)_3$ perovskite quantum dots in an ambient atmosphere: Stability analysis and self-powered photodetector applications. *New J. Chem.* **2023**, *47*, 13783–13788.
[15] Locardi, F.; Cirignano, M.; Baranov, D.; Dang, Z. Y.; Prato, M.; Drago, F.; Ferretti, M.; Pinchetti, V.; Fanciulli, M.; Brovelli, S. et al. Colloidal synthesis of double perovskite $Cs_2AgInCl_6$ and Mn-doped $Cs_2AgInCl_6$ nanocrystals. *J. Am. Chem. Soc.* **2018**, *140*, 12989–12995.
[16] Lavadiya, S.; Ahmed, M. S.; Barman, C.; Gupta, S. K.; Raavi, S. S. K. Temperature-dependent structure-property relationship of Mn-doped $Cs_2AgInCl_6$ thin films impacts its application as a self-powered UV photodetector. *ACS Appl. Electron. Mater.* **2024**, *6*, 2749–2758.
[17] Liu, M. N.; Ali-Löytty, H.; Hiltunen, A.; Sarlin, E.; Qudsia, S.; Smått, J. H.; Valden, M.; Vivo, P. Manganese doping promotes the synthesis of bismuth-based perovskite nanocrystals while tuning their band structures. *Small* **2021**, *17*, 2100101.
[18] Zhang, H. J.; Zhang, Y.; Li, X.; Zhang, J. M.; He, Y. J.; Yang, X.; Xu, J. T.; Jia, D. D.; Liu, J. Q. *In situ* synthesis of MnO/C nanoparticles anchored on reduced graphene oxide as high-performance zinc ion battery cathode with enhanced zinc storage performance. *J. Energy Storage* **2024**, *87*, 111331.
[19] Lin, Y. J.; Lee, J. Y.; Chen, S. M. Changing electrical properties of PEDOT:PSS by incorporating with dimethyl sulfoxide. *Chem. Phys. Lett.* **2016**, *664*, 213–218.
[20] Sebastia-Luna, P.; Gélvez-Rueda, M. C.; Dreessen, C.; Sessolo, M.; Grozema, F. C.; Palazon, F.; Bolink, H. J. Potential and limitations of $Csbi_3I_{10}$ as a photovoltaic material. *J. Mater. Chem. A* **2020**, *8*, 15670–15674.
[21] Liu, S. J.; Fang, H. W.; Su, S. H.; Li, C. H.; Cherng, J. S.; Hsieh, J. H.; Juang, J. Y. Physical properties of amorphous $InGaZnO_4$ films doped with Mn. *Appl. Phys. Lett.* **2009**, *94*, 092504.
[22] Ivanenko, L.; Filonov, A.; Shaposhnikov, V.; Behr, G.; Souptel, D.; Schumann, J.; Vinzelberg, H.; Plotnikov, A.; Borisenko, V. Transport properties of Mn-doped Ru_2Si_3. *Microelectron. Eng.* **2003**, *70*, 209–214.
[23] Zhao, Y. J.; Sun, Y. C.; Pei, C. X.; Yin, X.; Li, X. Y.; Hao, Y.; Zhang, M. R.; Yuan, M.; Zhou, J. L.; Chen, Y. et al. Low-temperature fabrication of stable black-phase $CsPbI_3$ perovskite flexible photodetectors toward wearable health monitoring. *Nano-Micro Lett.* **2025**, *17*, 63.
[24] Fang, Y. J.; Huang, J. S. Resolving weak light of sub-picowatt per square centimeter by hybrid perovskite photodetectors enabled by noise reduction. *Adv. Mater.* **2015**, *27*, 2804–2810.
[25] Zhao, Z. J.; Liu, B. Q.; Xie, C. L.; Ma, Y.; Wang, J.; Liu, M.; Yang, K. X.; Xu, Y. H.; Zhang, J.; Li, W. W. et al. Highly sensitive, sub-microsecond polymer photodetectors for blood oxygen saturation testing. *Sci. China Chem.* **2021**, *64*, 1302–1309.
[26] Du, Z. F.; Luong, H. M.; Sabury, S.; Jones, A. L.; Zhu, Z. Y.; Panoy, P.; Chae, S.; Yi, A.; Kim, H. J.; Xiao, S. et al. High-performance wearable organic photodetectors by molecular design and green solvent processing for pulse oximetry and photoplethysmography. *Adv. Mater.* **2024**, *36*, 2310478.
[27] Yokota, T.; Zalar, P.; Kaltenbrunner, M.; Jinno, H.; Matsuhisa, N.; Kitanosako, H.; Tachibana, Y.; Yukita, W.; Koizumi, M.; Someya, T. Ultraflexible organic photonic skin. *Sci. Adv.* **2016**, *2*, e1501856.
[28] Dcosta, J. V.; Ochoa, D.; Sanaur, S. Recent progress in flexible and wearable all organic photoplethysmography sensors for SpO_2 monitoring. *Adv. Sci.* **2023**, *10*, 2302752.
[29] Lou, Z. R.; Tao, J.; Wei, B. B.; Jiang, X. Y.; Cheng, S. M.; Wang, Z. H.; Qin, C.; Liang, R.; Guo, H. T.; Zhu, L. P. et al. Near-infrared organic photodetectors toward skin-integrated photoplethysmography-electrocardiography multimodal sensing system. *Adv. Sci.* **2023**, *10*, 2304174.